

Series resistance contribution of majority carriers in CELLO impedance analysis: Influence of wafer thickness variation



Jan-Martin Wagner*, Andreas Schütt, Jürgen Carstensen, Helmut Föll

Institute for Materials Science, Technical Faculty, University of Kiel, 24143 Kiel, Germany

ARTICLE INFO

Article history:

Received 25 August 2014

Received in revised form

25 August 2015

Accepted 17 November 2015

Keywords:

LBIC

CELLO impedance analysis

Wafer thickness map

High-efficiency silicon solar cells

PERC structure

Series resistance

ABSTRACT

Local series resistance measurements are an essential tool for optimization of silicon solar cells and cell concepts. This holds especially for nearly all advanced cell concepts where the minority carrier properties are improved at the expense of the majority ones (e.g., by a lower-doped emitter or point contacts at the back side). For such solar cells, frequency-dependent CELLO measurements allow an efficient series resistance characterization since they can e.g. distinguish ohmic losses originating in the volume of a solar cell from the total ohmic losses, thereby making it possible to identify wafer thickness variations. The thickness information allows to improve the reliability of fitting parameter results obtained from a CELLO impedance analysis and to identify other thickness-variation-related problems that may occur in the fabrication process.

© 2015 Elsevier B.V. All rights reserved.

1. Introduction

For many recent silicon solar cell concepts, an improved minority carrier yield is deliberately accompanied by a slightly worsened extraction of majority carriers, e.g. by an increased series resistance related to point contacts in a dielectric passivation layer at the back side or by a lower-doped emitter. For such solar cells, the investigation of ohmic losses has a higher relevance. Since they are larger than usual, these losses can be detected more easily, however they also need to be properly attributed to the relevant part of the solar cell. Here we demonstrate the possibility to distinguish the bulk-related ohmic losses from the total ohmic losses by means of a CELLO impedance analysis, using an augmented fit model for the phase shift related to the majority carrier flow in addition to that of the minority carriers.

2. Method: CELLO impedance analysis

2.1. Experimental

In the CELLO (solar CELLOcal characterization [1]) measurement technique, the linear current or voltage response of a solar cell to a modulated laser beam scanning the solar cell is mapped

while the solar cell is kept at a chosen working point of its (illuminated or dark) I - V curve. To that end, a standard 4-probe arrangement is used, i.e. the solar cell is contacted with separate leads for current supply and voltage measurement, all connected to a very fast electronic feed-back for either potentiostatic (for LBIC) or galvanostatic (for LBIV) measurement conditions.

The present CELLO set-up contains four lasers with different wavelengths: blue (405 nm), red (650 nm), and infrared (830 nm, denoted "IR"; 934 nm, denoted "SIR"), corresponding to penetration depths in silicon of about 100 nm, 4 μ m, 15 μ m, and 45 μ m, respectively. All lasers scan confocally over the sample (smallest focus size: 50 μ m) and can be modulated with different frequencies in the 10 kHz range. The corresponding small-signal linear response is obtained by an *in situ* software lock-in using fast Fourier transform analysis, enabling a measurement with up to four frequencies simultaneously. Additionally, higher (second) harmonics present in the photocurrent can be analyzed and mapped simultaneously with the linear response signal. Their measurement serves as a routine test for the applicability of the fit model described below.

Since the CELLO measurement system is time-calibrated, both amplitude and phase (time offset between excitation and response) are obtained. Compared to standard LBIC measurements, this enables very fast scans; for example, a short-circuit current response map with about 10^6 pixels can be obtained in roughly 15 min. Besides wafer-based silicon solar cells [1,2], also thin-film [3] and tandem structures [4] can be investigated by

* Corresponding author. Tel.: +49 431 8806181.

E-mail address: jwa@tf.uni-kiel.de (J.-M. Wagner).

CELLO to an unparalleled degree, yielding the individual problems involved (e.g., series resistance [5], current and/or voltage loss at maximum power point [2,3,6], current matching [4], parasitic shunting [7], injection level dependences [8], or shunts due to potential induced degradation [9]).

2.2. Theory and fit model

The CELLO measurement can be formally described by a complex transfer function Z , called impedance, that for each modulation (lock-in) frequency ω relates the small-signal linear response of the solar cell, measured e.g. as a photocurrent $I(\omega)$, to the corresponding laser excitation amplitude $P(\omega)$:

$$Z(\omega) := \frac{I(\omega)}{P(\omega)} \exp[i\phi(\omega)] = Z_0(\omega) \exp[i\phi(\omega)]. \quad (1)$$

Z_0 describes the amplitude of the response and the phase ϕ the time delay between excitation and response. By the measurement, these data are obtained for each scanning position of the laser beam, resulting in amplitude and phase-shift maps.

There are several contributions to this impedance [10], of which only those will be discussed here that are due to the solar cell under investigation; nevertheless, the influence of those being due to the measurement electronics itself is taken fully into account. The first contribution is due to the minority transport through the bulk, which can be described by the solution of the one-dimensional diffusion equation for complete extraction of the photocurrent, i.e. for the solar cell being held under short-circuit condition:

$$Z_{\min}(\tau, D, S_b, R_{\text{opt}}, \alpha, d_w, \omega) = \frac{qF(1 - R_{\text{opt}})}{1 - \left(\frac{1}{\alpha L}\right)^2} \frac{1 - \frac{S_b}{\alpha D} + \left(\frac{\tilde{L} S_b}{D} - \frac{1}{\alpha L}\right) \tanh\left(\frac{d_w}{L}\right)}{1 + \frac{\tilde{L} S_b}{D} \tanh\left(\frac{d_w}{L}\right)}. \quad (2)$$

The parameters have the following meaning: bulk lifetime τ , minority diffusion coefficient D (related to their mobility μ by the Einstein relation $D = \frac{kT}{q}\mu$), back-surface recombination velocity S_b , reflectivity R_{opt} , silicon light absorption coefficient α , wafer thickness d_w , and laser modulation frequency ω . On the right-hand side, qF is the elementary charge times the optical flux from the laser beam. The modulation frequency enters through \tilde{L} , the effective diffusion length; with the usual diffusion length $L = \sqrt{D\tau}$, it follows directly from the frequency-dependent diffusion equation as

$$\tilde{L} = \frac{L}{\sqrt{1 + i\omega\tau}} = \sqrt{D} / \sqrt{1 + i\omega\tau}. \quad (3)$$

Second, there is a contribution of the majority carrier flow. Since the transport of the majority carriers is very fast, up to now the simplest model for Z_{maj} was used, which can be most easily obtained as follows. For linear response measurements at a certain working point of the I - V characteristic, the diode in the equivalent circuit of a solar cell can be replaced by a parallel circuit of a capacitor C_D and an ohmic resistor R_D , the latter representing the linearized characteristic at the chosen working point; see Fig. 1.

Under short-circuit condition, the diode resistance is very high, so that R_D can be neglected (i.e., taken to be infinity), and the photocurrent passes a parallel circuit of the series resistance R_{ser} of the illuminated spot and the corresponding p-n junction capacity C_D , which results in

$$Z_{\text{maj}} = \frac{1}{1 + i\omega R_{\text{ser}} C_D}. \quad (4)$$

This leads to a phase shift of

$$\varphi_{\text{maj}} \approx \tan \varphi_{\text{maj}} = -\omega R_{\text{ser}} C_D, \quad (5)$$

i.e. proportional to the modulation frequency.

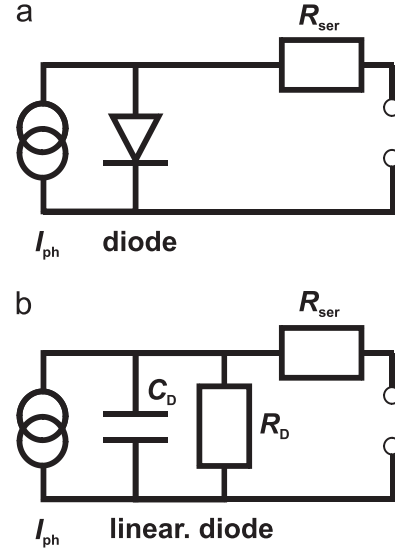


Fig. 1. (a) Standard equivalent circuit of a solar cell, neglecting shunts; (b) ditto modified for linear response.

The total impedance relevant for the solar cell physics is given by $Z = Z_{\min} \times Z_{\text{maj}}$. In general, the information contained in measured phase-shift map ϕ varies with the modulation frequency, since the processes involved are dominant at different frequencies [11]. For two measurements taken with the same laser but with different modulation frequencies, this information can be reduced by calculating the following difference map with the phase shifts converted to absolute delay times [12]:

$$\Delta_{\text{lin}} = \frac{\varphi(\omega_1)}{\omega_1} - \frac{\varphi(\omega_2)}{\omega_2}. \quad (6)$$

In the map resulting from Eq. (6), all phase shift contributions depending linearly on the modulation frequency will be eliminated. Since this includes the $R_{\text{ser}} C_D$ phase shift of the majorities according to Eq. (5), the resulting map can contain majority carrier information beyond the Z_{maj} model, Eq. (4).

A fit of a set of short-circuit current data (amplitude and phase), obtained from different lasers and measured for different modulation frequencies, to the impedance model, Eqs. (2) and (4) (= impedance analysis), allows to derive maps of the involved electrical and material-related parameters of interest (e.g. minority carrier lifetime τ , back-surface recombination velocity S_b , diffusion coefficient D , $R_{\text{ser}} C_D$ time constant). This procedure was used successfully for different solar cells with various problems involved, e.g. mobility variations [2], inhomogeneous back-surface field formation [2,11], strongly injection-level-dependent parameters [8], or mechanical stress [13].

3. Samples

The measurements were made on small (2 cm × 2 cm) p-type multicrystalline silicon solar cells fabricated by a lab-type process at the University of Konstanz, Germany [14]. At the front side these plasma-textured cells feature a POCl_3 emitter (80 Ω/sq) and an evaporated Ti/Pd/Ag metal grid with a collecting bus bar at one side with the main contact at its center. PECVD silicon nitride serves as anti-reflection coating, surface passivation and source of hydrogen for bulk defect passivation during a firing step. At the back side the cells have a PERC-type structure with laser fired Al point contacts and a dielectric passivation layer consisting of an aluminum oxide / silicon nitride stack.

4. Results and discussion I: measured data

Fig. 2 exemplarily shows amplitude and phase-shift maps of the three different lasers, all taken with a modulation frequency of about 6.6 kHz and a resolution of 30 pixel/mm, for sample A. As noted in [11], at this low modulation frequency the influence of the bulk lifetime (noticeable in all maps, e.g. at recombination-active grain boundaries and at the left edge) and of the back-surface recombination velocity (noticeable only in the IR and SIR maps) dominate the photocurrent losses. Due to the large penetration depth of the SIR laser, the point contacts at the back side are most clearly visible in Fig. 2(c). Also some minor isolated defects, extending over few point contacts, are best visible in the SIR maps and are present in the IR maps, but are hardly noticeable in the red laser maps. The largest phase-shift values are found in the lower right part of the sample.

Fig. 3 shows the delay-time differences according to Eq. (6), calculated from the phase-shift maps taken at about 6.6 kHz and 22 kHz, for sample A. Additionally, in Fig. 3(d) locally measured sample thicknesses are given in μm . In the lower right part the thickness is largest. Most astonishingly, in contrast to Fig. 2, the point contacts are not visible anymore. The large-scale variation (over several mm) in the maps is identical for all lasers, and this variation corresponds very well to the measured local cell thicknesses. The relative strength of this thickness-correlated large-scale variation shows a clear trend with the laser wavelength: it is most pronounced for the SIR, less pronounced for the IR, and only slightly visible for the red laser.

The fact that the point contacts at the back side are not visible in those regions of Fig. 3 that exhibit the thickness-correlated variation means that in those regions there is no influence from the minority recombination at the back side. This is a first hint that the thickness variation seen here is not due to the minority, but due to the majority carriers. (It also indicates that the quality and the homogeneity of the point contacts is very good.) A second hint in the same direction is the observed thickness contrast variation with the laser wavelength: The SIR laser has the largest penetration depth, so the distance for the laser-generated majorities to reach the back side is smallest for this laser, and therefore wafer thickness variations have the largest influence. The smaller the

laser penetration depth, the larger the distance to the back side, and therefore the smaller the relative influence of thickness variations. A third hint comes from the absolute values of the phase-shift data in Fig. 2, which are smallest for the red laser, indicating smallest distances traveled by the minorities, therefore for this laser the thickness-correlated information in Fig. 3 can only be due to the majority carriers.

The lowest-frequency second harmonic of the red and IR laser, Fig. 4(a) and (b), shows a small and nearly homogeneous signal. Maps of second harmonics for higher frequencies of these lasers (not shown) are also small and look similar. The lowest-frequency second harmonic of the SIR laser shows a large-scale inhomogeneity, but overall is also small. Second harmonics for higher frequencies of the SIR laser show this large-scale inhomogeneity in different markedness; all such signals are small. “Small” means in all cases that the nonlinear signal is in the order of 1% of the corresponding linear signal. As discussed in [8], this standard test indicates that nonlinear effects in the sample are negligible so that it is justified to use the impedance fit model to extract maps of separate electrical and material-related parameters. Fig. 4 furthermore shows that the thickness-correlated variation in Fig. 3 is not due to nonlinear effects.

5. Results and discussion II: impedance fits

5.1. Sample A

A fit of the full set of measured data – which here consists of 24 maps, namely amplitude and phase shift of the red, IR, and SIR laser, all taken for four different modulation frequencies – to the standard impedance model, Eqs. (2), (3) and (4), gave unsatisfactory results. A closer look at the measured phase shift data shows that the large-scale variation visible in Fig. 3 is due to a sub-linear frequency dependence, with the deviation from linearity mainly showing a quadratic behavior. (This furthermore shows that the large-scale variation visible in Fig. 3 is not due to a nonlinear effect, since the latter would exhibit a 2ω frequency dependence; cf. the data shown in Fig. 4). Several attempts to use an accordingly modified fit model for the minorities were not successful. Fitting not the whole data set

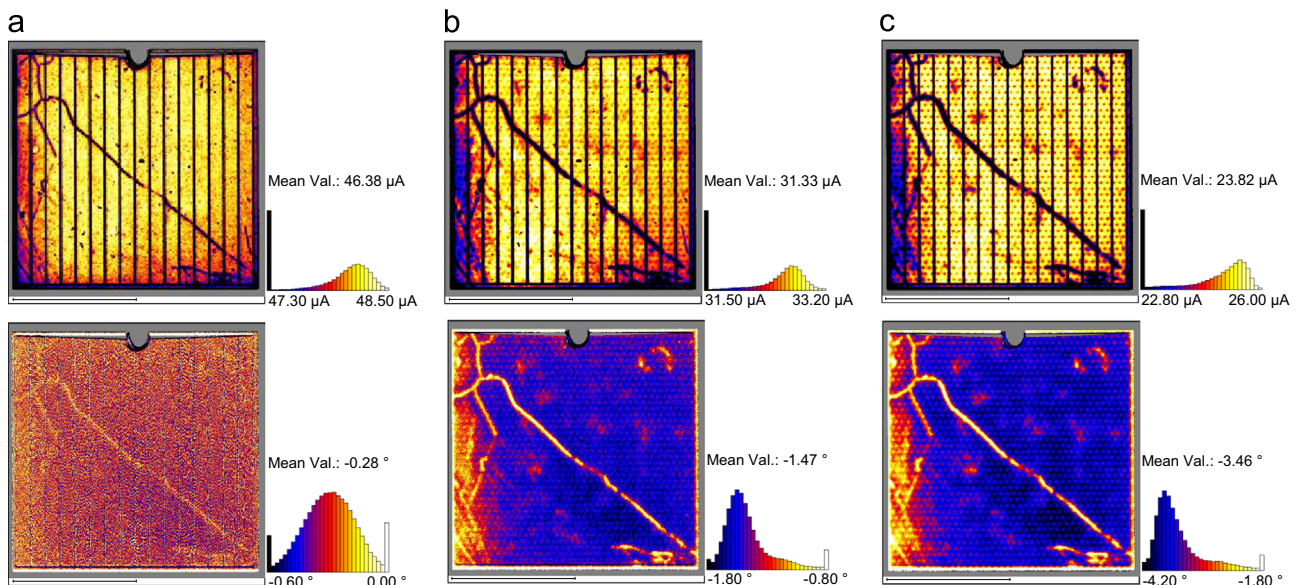


Fig. 2. CELLO short-circuit current maps of sample A, all taken at 6.6 kHz laser modulation frequency. Top row: amplitude, bottom row: phase shift. (a) Red laser; (b) IR laser; (c) SIR laser. The scale bar below the maps represents one centimeter. (For interpretation of the references to color in this figure legend, the reader is referred to the web version of this article.)

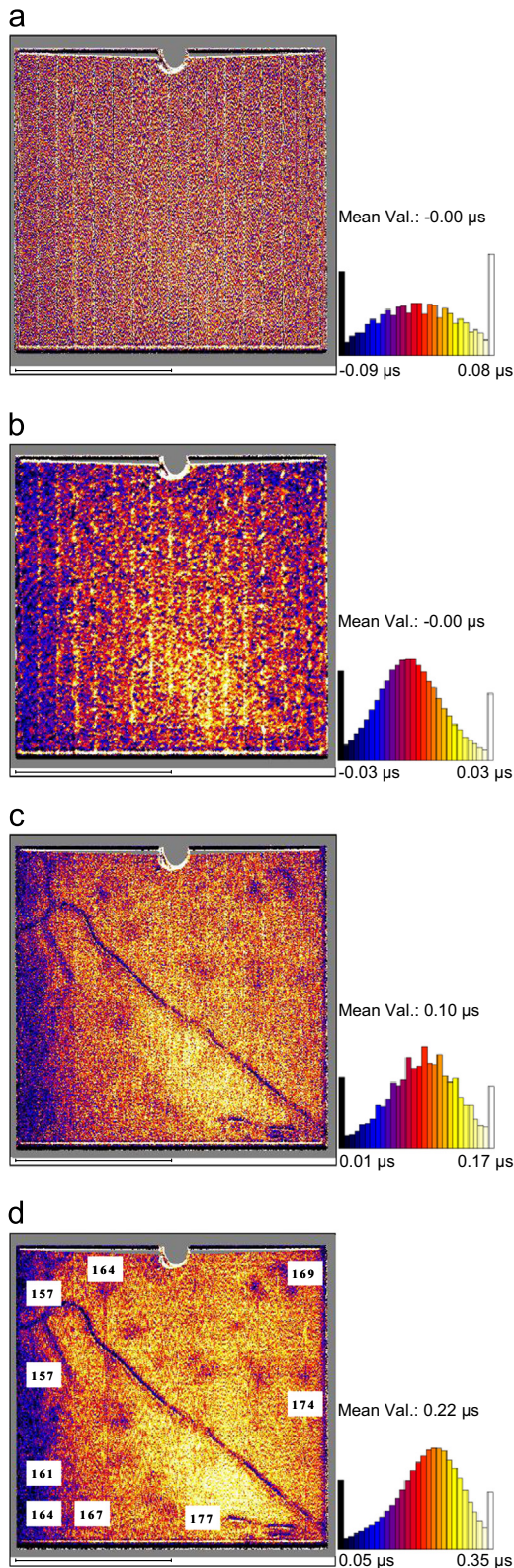


Fig. 3. Differences of phase-shift maps, taken at about 6.6 kHz and 22 kHz and converted to delay times [Δ_{lin} , cf. Eq. (6)], for sample A. (a) Red laser; (b) same data as (a), slightly smoothed; (c) IR laser; (d) SIR laser. The numbers overlaid in (d) are locally measured thicknesses at the cell edge in μm . The scale bar below the maps represents one centimeter. (For interpretation of the references to color in this figure legend, the reader is referred to the web version of this article.)

but just those of a single laser gave much better results, showing a systematic dependence on the laser wavelength for the majority impedance ($R_{\text{ser}}C_D$ time constant). This is a further hint that the

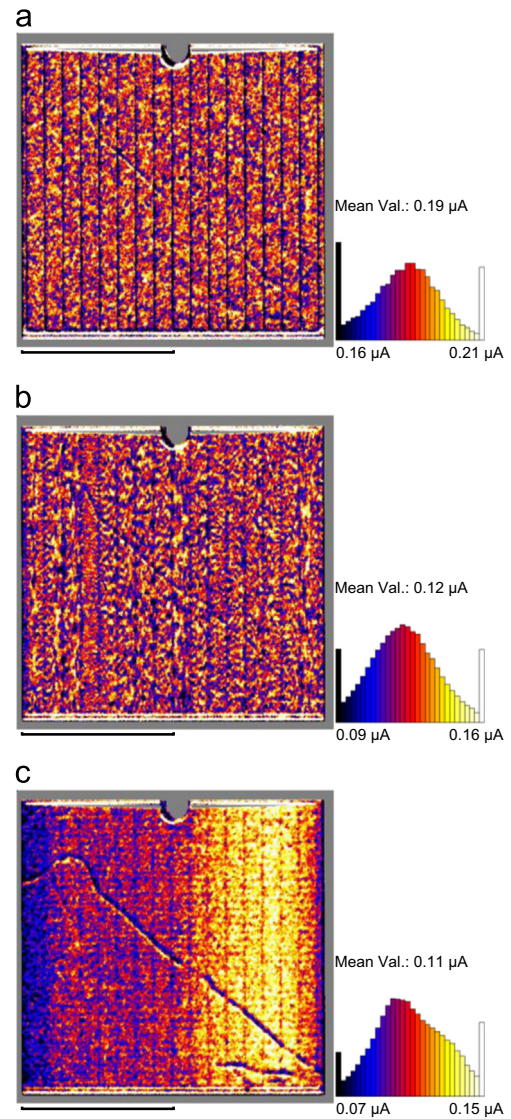


Fig. 4. Lowest-frequency second harmonic amplitude maps, taken at 13.2 kHz; data slightly smoothed. (a) Red laser, (b) IR laser, (c) SIR laser. No correlation with the thickness variation [overlaid numbers in Fig. 3(d)] is found. The scale bar below the map represents one centimeter. (For interpretation of the references to color in this figure legend, the reader is referred to the web version of this article.)

observed thickness variation and, therefore, the phase contribution with a quadratic frequency dependence, is due to the majority carriers.

Putting together all information obtained so far, a modified fit model for the majority carriers was introduced empirically, explicitly taking into account the observed quadratic frequency dependence:

$$\tilde{Z}_{\text{maj}} = \frac{1}{1 + i\omega R_{\text{ser}}C_D - i\omega^2 B f(\alpha, d_w)} \quad (7)$$

The dependence of the newly introduced “quadratic term” on the laser wavelength (expressed by the absorption coefficient α) and on the wafer thickness, contained in the function $f(\alpha, d_w)$, was treated by a simple geometrical model for the distances relevant for the majority carriers generated by the local laser spot illumination to reach the point contacts at the back side, leaving a single factor B as fit parameter. Thereby, the “quadratic term” can be interpreted as representing the bulk-related ohmic losses.

This model allowed a satisfying fit of the whole data set measured, i.e. a consistent description was obtained by Eq. (7).

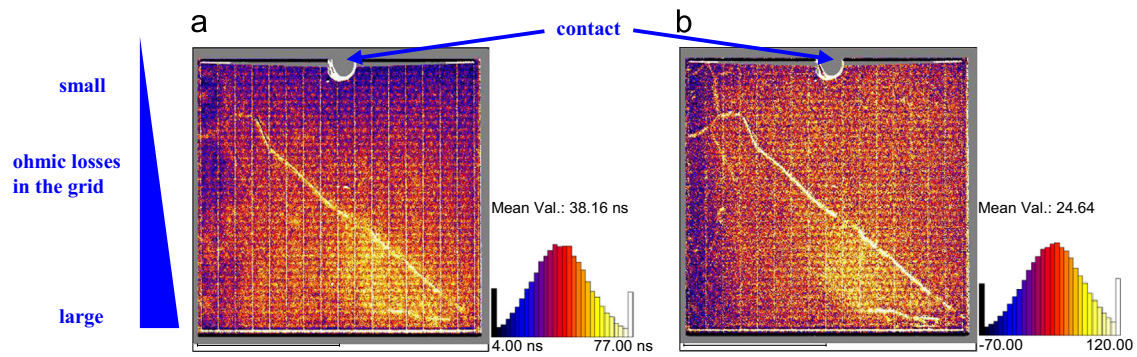


Fig. 5. Impedance fit results for sample A, using the modified model of Eq. (7) for the majorities. (a) $R_{ser}C_D$ time constant; (b) bulk-related ohmic losses as described by B in Eq. (7). The scale bar below the maps represents one centimeter. (For interpretation of the references to color in this figure legend, the reader is referred to the web version of this article.)

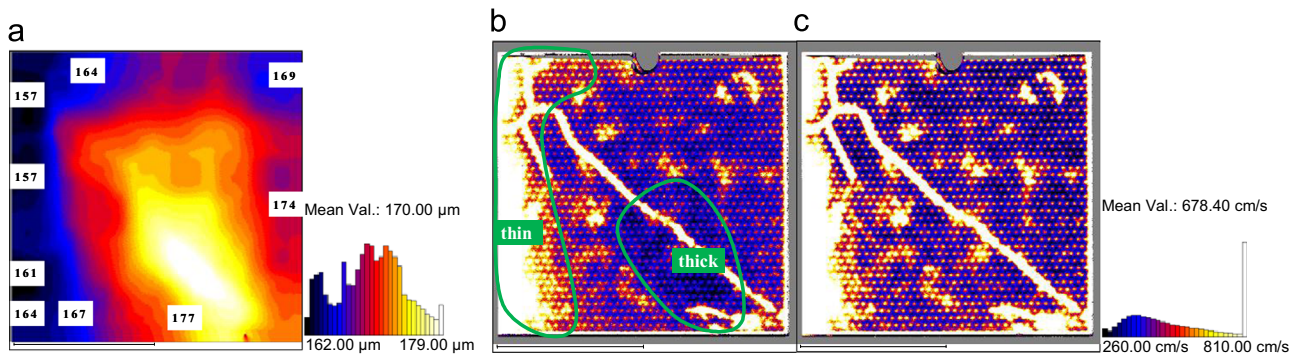


Fig. 6. Impedance fit results for sample A. (a) Thickness distribution obtained from Fig. 5(b), together with locally measured thicknesses at the cell edge in μm ; (b) standard impedance fit model result for S_b , based on a constant cell thickness; (c) S_b result taking into account the thickness variation of the cell. The scale bar below the maps represents one centimeter. (For interpretation of the references to color in this figure legend, the reader is referred to the web version of this article.)

Together with the fact that no other fitting attempt led to such a result, this is a further, strong hint that the phase contribution with a quadratic frequency dependence is due to the majority carriers. The results for the majorities obtained from this consistent fit are shown in Fig. 5.

Fig. 5(a) shows the standard $R_{ser}C_D$ time constant, it shows a mixture of local and long-range variations. The systematic trend of values increasing from the upper part to the lower part (schematically indicated by the triangle next to the map) can be understood from the grid geometry, having a single contact at the top center in the image and therefore leading to the observed increase in the ohmic losses towards the lower edge.

Fig. 5(b) shows the amplitude of the “quadratic term”, i.e. the bulk-related ohmic losses. As discussed for Fig. 3, the long-range variation found in Fig. 5(b) represents the wafer thickness. In the area with the largest thickness, also the standard $R_{ser}C_D$ time constant shows the largest values, which therefore can be simply understood as a trivial consequence of increased ohmic losses for majority carriers drifting through the bulk of the solar cell and otherwise homogeneous properties of the solar cell.

Using the known average wafer thickness of $170\ \mu\text{m}$ and the thickness variation information contained in the long-range variation of Fig. 5(b) results in the thickness distribution shown in Fig. 6(a).

Fig. 6(a) shows a very good agreement with the data measured directly at the cell edge. This thickness map has been used to improve the fit for the minority properties: Fig. 6(b) shows S_b obtained for the wafer thickness assumed to be constant, and Fig. 6(c) shows S_b taking into account the actual cell thickness of Fig. 6(a). The latter result is significantly more homogeneous, not

showing the thickness-related artifact in the lower right part seen in Fig. 6(b).

5.2. Sample B

For a second sample of the same kind, the thickness variation was obtained from an impedance fit in the same way as described above; the result is shown in Fig. 7(a), together with directly measured data. The standard result for S_b is shown in Fig. 7(b).

Also for sample B, the thickness distribution obtained from the impedance fit, Fig. 7(a), shows a good agreement with directly measured data. In general, there is a certain similarity in the overall thickness distribution between Fig. 6(a) and Fig. 7(a) in that the region of largest thickness is of rectangular shape with similar proportions and that the thinnest side of the wafer is found alongside that region, indicating that both cells come from the same fabrication process.

Certain stripes of significantly increased S_b values in Fig. 7(b) are found only in the area with increased thickness. This indicates that the thickness variations lead (directly or indirectly) to the worsened dielectric passivation. Since the thickness variation is due to an etching process, this means that also the worsened dielectric passivation can be related to the etching process.

6. Conclusion and summary

An additional quadratic dependency of the phase shift on the modulation frequency found in CELLO short-circuit current measurements on high-efficiency multicrystalline silicon solar cells,

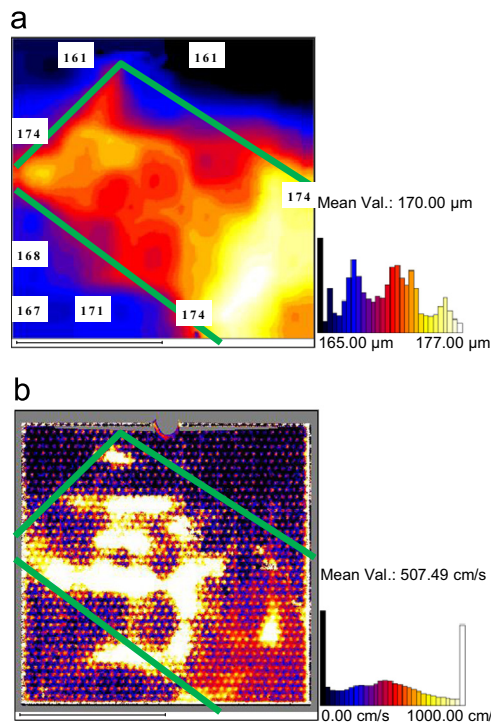


Fig. 7. Impedance fit results for sample B. (a) Thickness distribution analogous to Fig. 6(a), together with locally measured thicknesses at the cell edge in μm ; (b) standard model result for S_b , based on a constant cell thickness. The brown lines indicate the area with the largest thickness. The scale bar below the maps represents one centimeter. (For interpretation of the references to color in this figure legend, the reader is referred to the web version of this article.)

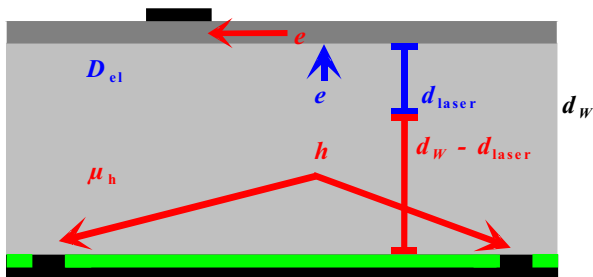


Fig. 8. Schematic representation of a p-type Si solar cell having point contacts in a dielectrically passivated back side (green). Red symbols and quantities: related to majority carriers, blue symbols and quantities: related to minority carriers. d_w : wafer thickness, d_{laser} : laser penetration depth ($=1/\alpha$), D_{el} : diffusion coefficient of the electrons, μ_h : hole mobility. The deeper inside the wafer the holes are generated, the shorter are their paths and, correspondingly, the smaller are their ohmic losses for reaching the back contacts. (For interpretation of the references to color in this figure legend, the reader is referred to the web version of this article.)

showing a systematic variation with the laser wavelength (and, therefore, with the penetration depth of the laser light), has been successfully attributed to the majority carrier flow by a fit model considering the distances relevant for the laser-spot-generated majority carriers to reach the back side; the corresponding geometrical considerations are summarized in Fig. 8.

Although the presented results are preliminary ones and a detailed modeling of the quadratic frequency dependence is yet to come, already a consistent description was obtained and relevant conclusions can be drawn for solar cell concepts where minority carrier properties are improved at the expense of the majority ones, e.g. with dielectric back side passivation and point contacts, leading to longer distances for the majorities to reach the back

side. The thickness information derived from the analysis of the additional quadratic frequency dependence was shown to be very helpful to improve the reliability of local fitting parameters like S_b obtained from a CELLO impedance analysis and to identify other thickness-variation-related problems that may occur in the fabrication process. Interestingly, the additional quadratic frequency dependence was observed for high-quality samples with low S_b and no contact resistance problems; a few years ago, the samples were not of such quality, and the effect was not noticed.

Acknowledgments

This work was supported by the DFG (German Research Foundation) under Grant FO 258/11-2. We thank the group of Giso Hahn, University of Konstanz, Germany, for providing the samples, and we thank Rainer Adelung for continuing the solar cell research work at our institute.

References

- [1] J. Carstensen, G. Popkurov, J. Bahr, H. Föll, CELLO: an advanced LBIC measurement technique for solar cell local characterization, *Sol. Energy Mater. Sol. Cells* 76 (2003) 599–611.
- [2] J. Carstensen, A. Schütt, G. Popkurov, H. Föll, CELLO measurement technique for local identification and characterization of various types of solar cell defects, *Phys. Status Solidi C* 8 (2011) 1342–1346.
- [3] J.-M. Wagner, J. Carstensen, A. Schütt, H. Föll, Qualitative and quantitative evaluation of thin-film solar cells using solar cell local characterization, *J. Appl. Phys.* 113 (2013) 064503-1–064503-4.
- [4] A. Schütt, J. Carstensen, J.-M. Wagner, H. Föll, M. Nguyen, S. Klein, Spectrally resolved local CELLO characterization of tandem solar cells using linear and 2nd harmonic response analysis, In: Proceedings of the 27th European Photovoltaic Solar Energy Conference, Frankfurt, Germany, 2012, pp. 2598–2603.
- [5] J. Carstensen, A. Schütt, H. Föll, CELLO local solar cell resistance maps: modeling of data and correlation to solar cell efficiency, In: Proceedings of the 22nd European Photovoltaic Solar Energy Conference, Milan, Italy, 2007, pp. 337–340.
- [6] A. Schütt, J. Carstensen, H. Föll, S. Keipert-Colberg, D. Borchert, Evaluation of passivation schemes of large area Si solar cells: separating serial resistance from other losses by the CELLO technique, In: Proceedings of the 26th European Photovoltaic Solar Energy Conference, Hamburg, Germany, 2011, pp. 1534–1537.
- [7] A. Schütt, J. Carstensen, H. Föll, S. Keipert-Colberg, D. Borchert, CELLO analysis of solar cells with silicon oxide/silicon nitride rear side passivation: parasitic shunting, surface recombination, and series resistance as rear side influences, In: Proceedings of the 27th European Photovoltaic Solar Energy Conference, Frankfurt, Germany, 2010, pp. 1368–1372.
- [8] J. Carstensen, A. Schütt, G. Popkurov, H. Föll, CELLO FFT impedance analysis of solar cells with a strong injection level dependence, In: Proceedings of the 25th European Photovoltaic Solar Energy Conference, Valencia, Spain, 2010, pp. 2160–2163.
- [9] A. Schütt, J. Carstensen, J.-M. Wagner, H. Föll, Influence of surface and process induced defects on potential-induced degradation and regeneration, In: Proceedings of the 28th European Photovoltaic Solar Energy Conference, Paris, France, 2013, pp. 831–835.
- [10] A. Schütt, S. Keipert, J. Carstensen, H. Föll, Modeling of the frequency dependence of the CELLO photo current for increasing measurement speed and identification of defect types, In: Proceedings of the 22nd European Photovoltaic Solar Energy Conference, Milan, Italy, 2007, pp. 341–344.
- [11] J. Carstensen, A. Schütt, H. Föll, CELLO measurements with FFT impedance analysis: drastic increase of measurement speed for analysis of local solar cell defects, In: Proceedings of the 23rd European Photovoltaic Solar Energy Conference, Valencia, Spain, 2008, pp. 73–76.
- [12] J. Carstensen, A. Schütt, A. Pape, H. Föll, CELLO measurements for local and global characterization of grid finger, contact, and emitter resistance losses of large area solar cells, In: Proceedings of the 25th European Photovoltaic Solar Energy Conference, Valencia, Spain, 2010, pp. 2134–2137.
- [13] A. Schütt, J. Carstensen, G. Popkurov, H. Föll, Mechanical stress induced effects for the characterization of large area solar cells, In: Proc. of the 26th European Photovoltaic Solar Energy Conference, Hamburg, Germany, 2011, pp. 1182–1186.
- [14] J. Junge, J. Ebser, S. Graf, B. Terheiden, S. Seren, G. Hahn, M. Käs, Evaluating the efficiency limits of low cost mc Si materials using advanced solar cell processes, In: Proceedings of the 25th European Photovoltaic Solar Energy Conference, Valencia, Spain, 2010, pp. 1722–1726.